


## RESEARCH ARTICLE

# From non-doped to dopable: The impact of methoxy functionalization on doping and thermoelectric properties of conjugated polymers

Hansol Lee<sup>1</sup> | Landep Ayuningtias<sup>2</sup> | Hoimin Kim<sup>3</sup> | Jaehoon Lee<sup>3</sup> |  
 Jiyun Lee<sup>3</sup> | Min-Jae Kim<sup>3</sup> | Dongki Lee<sup>4</sup> | Byung Mook Weon<sup>5</sup> |  
 Dong-Am Park<sup>6</sup> | Nam-Gyu Park<sup>6</sup> | Sung Yun Son<sup>7</sup> | Junki Kim<sup>3,8</sup> |  
 Yun-Hi Kim<sup>2</sup> | Boseok Kang<sup>3,8</sup> 

<sup>1</sup>Department of Chemical and Biological Engineering, Gachon University, Seongnam, Republic of Korea

<sup>2</sup>Department of Chemistry and Research Institute of Natural Science (RINS), Gyeongsang National University, Jinju, Republic of Korea

<sup>3</sup>SKKU Advanced Institute of Nanotechnology (SAINT) and Department of Nano Science and Technology, Sungkyunkwan University, Suwon, Republic of Korea

<sup>4</sup>Department of Nanotechnology and Advanced Materials Engineering, Sejong University, Seoul, Republic of Korea

<sup>5</sup>School of Advanced Materials Science and Engineering and SKKU Advanced Institute of Nanotechnology (SAINT), Sungkyunkwan University, Suwon, Republic of Korea

<sup>6</sup>School of Chemical Engineering, Center for Antibonding Regulated Crystals and SKKU Institute of Energy Science and Technology (SIEST), Sungkyunkwan University (SKKU), Suwon, Republic of Korea

<sup>7</sup>Department of Chemistry, Kwangwoon University, Seoul, Republic of Korea

<sup>8</sup>Department of Nano Engineering, Sungkyunkwan University, Suwon, Republic of Korea

## Correspondence

Yun-Hi Kim, Department of Chemistry and Research Institute of Natural Science (RINS), Gyeongsang, National University, Jinju, 52828, Republic of Korea.  
 Email: [ykim@gnu.ac.kr](mailto:ykim@gnu.ac.kr)

Junki Kim and Boseok Kang, SKKU Advanced Institute of Nanotechnology (SAINT) and Department of Nano Science and Technology, Sungkyunkwan University, Suwon 16419, Republic of Korea.  
 Email: [junki.kim.q@skku.edu](mailto:junki.kim.q@skku.edu) and [bskang88@skku.edu](mailto:bskang88@skku.edu)

## Funding information

National Research Foundation of Korea (NRF), Grant/Award Numbers: 2021R1A2B5B03086367, 2022M3J7A1062940, 2023R1A2C1005015,

## Abstract

The introduction of alkoxy side chains into the backbone of conjugated polymers is an effective way to change their properties. While the impact on the structure and optoelectronic properties of polymer thin films was well-studied in organic solar cells and transistors, limited research has been conducted on their effects on doping and thermoelectric properties. In this study, the effects of methoxy functionalization of conjugated backbones on the doping and thermoelectric properties are investigated through a comparative study of diketopyrrolopyrrole-based conjugated polymers with and without methoxy groups (P29DPP-BTOM and P29DPP-BT, respectively). Methoxy-functionalization significantly enhances doping efficiency, converting undopable pairs to dopable ones. This dramatic change is attributed to the structural changes in the polymer film caused by the methoxy groups, which increases the lamellar spacing and facilitates the incorporation of dopants within the polymer crystals. Moreover, methoxy-functionalization is advantageous in

Hansol Lee, Landep Ayuningtias, and Hoimin Kim have contributed equally to this work.

This is an open access article under the terms of the [Creative Commons Attribution](https://creativecommons.org/licenses/by/4.0/) License, which permits use, distribution and reproduction in any medium, provided the original work is properly cited.

© 2024 The Authors. *EcoMat* published by The Hong Kong Polytechnic University and John Wiley & Sons Australia, Ltd.

RS-2022-00166297; International Research & Development Program of the NRF, Grant/Award Number: 2022K1A4A7A04094482

improving the Seebeck coefficient and power factor of the doped polymers, because it induces a bimodal orientational distribution in the polymer, which contributes to the increased splitting of Fermi and charge transport levels. This study demonstrates the impact of methoxy-functionalization of a conjugated polymer on doping behavior and thermoelectric properties, providing a guideline for designing high-performance conjugated polymers for thermoelectric applications.

#### KEYWORDS

conjugated polymers, doping efficiency, methoxy functionalization, molecular doping, organic thermoelectrics

## 1 | INTRODUCTION

Organic thermoelectrics based on conjugated polymers have drawn significant attention owing to their unique advantages such as solution-based low-cost manufacturing, light weight, flexibility, and inherently low thermal conductivity.<sup>1–4</sup> The primary performance metric in organic thermoelectric devices is typically represented by the power factor (PF), which is determined by the electrical conductivity ( $\sigma$ ) and Seebeck coefficient ( $S$ ), i.e.,  $PF = S^2\sigma$ . The performance limiting factor of most organic thermoelectric materials is their low electrical conductivity. Therefore, achieving high electrical conductivity through chemical doping of conjugated polymers using molecular dopants has been intensively studied in the field of organic thermoelectrics.<sup>2,5,6</sup> In addition, as the Seebeck coefficient exhibits a trade-off relationship with electrical conductivity, overcoming this trade-off and simultaneously improving the electrical conductivity and Seebeck coefficient are important challenges to be addressed.<sup>7,8</sup> Recently, significant progress has been made in improving the thermoelectric performance of conjugated polymers, accompanied by the development of novel conjugated polymers and their doping methods.

Engineering the molecular structure is of primary importance in the development of conjugated polymers with high thermoelectric performance because various properties of conjugated polymers, such as molecular conformation, inter- and intramolecular interactions, electronic structure, molecular packing, morphology of the polymer film, and chemical doping behavior, depend critically on the molecular structure of the polymer. An effective way to control the molecular structure is to introduce an alkoxy group into the backbone of conjugated polymers.<sup>9</sup> Tuning the alkyl side chains, which are the most commonly used side chains, can effectively modify the structure and properties of polymers by varying their length, branching, and side chain density; in

addition to this, the introduction of alkoxy side chains offers additional opportunities to control the properties of the polymer.<sup>10–15</sup> For example, the electron-donating characteristics of the alkoxy group can increase the molecular energy levels of a conjugated polymer. Particularly in donor-acceptor (D-A) type conjugated copolymers, the presence of alkoxy groups facilitates intramolecular charge transfer, consequently leading to a reduction in the band gap of the polymer.<sup>16,17</sup> The oxygen atom in an alkoxy side chain has decreased steric hindrance compared to the  $\text{CH}_2$  moiety of an alkyl side chain, owing to its smaller van der Waals radius. This phenomenon results in increased flexibility of the alkoxy side chains compared to alkyl side chains with similar structures.<sup>9</sup> Further, the oxygen atom can participate in intramolecular non-covalent interactions, such as S(thienyl)⋯O(alkoxy) interactions, which can contribute to an increase in the planarity of the conjugated polymer backbone.<sup>11,15</sup> Because of these functionalities, alkoxy functionalization of the conjugated polymer backbones has been reported to improve the performance of conjugated polymers in organic electronic devices, such as organic photovoltaics (OPVs) and organic field-effect transistors (OFETs).<sup>9,18</sup> However, the effects of alkoxy functionalization have been relatively less investigated in the field of organic thermoelectrics; therefore, further systematic studies of these effects are required.

Previous studies on the effect of alkoxy functionalization on doping and thermoelectric properties of conjugated polymers focused mainly on two functions of alkoxy side chains, raising the energy levels of the polymer and tuning the polarity of the side chains. The raised molecular energy level of the polymer by alkoxy side chains led to greater energetic driving force for electron transfer from the polymer to dopant.<sup>19–21</sup> Introduction of polar alkoxy side chains (e.g., oligoethylene glycol groups) enhanced the compatibility of dopants with the side chains, resulting in the increased miscibility of the

polymer and dopants.<sup>20–23</sup> These changes contributed to improved doping efficiency and thermoelectric performance of the alkoxy functionalized polymers. Although these studies have revealed the important functions of alkoxy side chains, they still have some limitations. One is that only limited structures of alkoxy side chains have been explored compared to the great variety of structures that alkoxy side chains can take, and another is that it is not well established to what extent the alkoxy functionalization effects can vary depending on the structure of the dopant used. Therefore, further insights can arise from the investigations on the conjugated polymers possessing alkoxy side chains with various structures combined with detailed microstructural analysis on doped polymer films for various polymer-dopant systems.

In this work, we investigated the effect of methoxy functionalization of the backbone of a D-A type conjugated copolymer based on diketopyrrolopyrrole (DPP) and bithiophene (BT) units. Through a comparative study of a methoxy-functionalized polymer and its non-methoxy-functionalized counterparts, we show that merely introducing short methoxy groups on the polymer backbone can cause significant change in doping characteristics of the polymer. The lamellar stacking distance of the polymer was significantly increased by the introduction of methoxy groups, which led to a significant increase in the doping efficiency due to the facilitated diffusion of the dopant molecules within the polymer crystals through the increased space between the stacked alkyl side chains. This effect became more pronounced with larger dopant molecule, resulting in the efficient doping of the methoxy-functionalized polymer by a large-sized dopant, while the same dopant exhibited an inability to dope the non-methoxy-functionalized polymer. In addition, the introduction of methoxy groups affected the molecular orientation distribution of the polymer films, which contributed to higher Seebeck coefficients of the methoxy-functionalized polymer than that of the polymer without methoxy groups for a given electrical conductivity. Consequently, the methoxy-functionalized polymer showed higher optimized thermoelectric performance compared to the non-methoxy-functionalized one.

## 2 | RESULTS AND DISCUSSION

Two D-A type conjugated copolymers, poly[2,5-bis(7-decylnonadecyl)pyrrolo[3,4-*c*]pyrrole-1,4(2*H*,5*H*)-dione-*alt*-5,5'-bis(thiophen-2-yl)-[2,2'-bithiophene] (P29DPP-BT) and poly[2,5-bis(7-decylnonadecyl)pyrrolo[3,4-*c*]pyrrole-1,4(2*H*,5*H*)-dione-*alt*-5,5'-bis(thiophen-2-yl)-[3,3'-dimethoxy-2,2'-bithiophene] (P29DPP-BTOM) were prepared by the Stille coupling reaction of their monomers (Figures 1a and

S1–S5). Details of the synthetic procedures are described in the Experimental Section of the Supporting Information. The number average molecular weights ( $M_n$ ) and polydispersity indices (PDIs) of the polymers were determined by gel permeation chromatography (GPC). The results are shown in Figure S6 and Table 1. The polymers showed good solubility in common organic solvents such as chloroform and chlorobenzene. The polymers also showed good thermal stability, with high thermal decomposition temperatures ( $T_d$ , the temperature at which 5% weight loss occurs) of  $\sim 404$  and  $364^\circ\text{C}$  for P29DPP-BT and P29DPP-BTOM, respectively (Figure S7), as characterized by thermogravimetric analysis (TGA). This trend of the polymers with methoxy groups on their backbones to exhibit lower degrees of thermal stability is in good agreement with previous reports.<sup>24,25</sup> The polymers did not exhibit thermal transitions in the differential scanning calorimetry (DSC) measurements up to  $300^\circ\text{C}$  (Figure S8). Their physical characteristics are summarized in Table 1.

In P29DPP-BT and P29DPP-BTOM, the BT unit and DPP unit with two flanked thiophenes were chosen as the donor and acceptor moieties, respectively. The core of DPP is strongly electron-deficient, which makes the DPP unit suitable as an acceptor group for constructing D-A type conjugated copolymers. Moreover, DPP-based conjugated polymers often exhibit strong interchain interactions and aggregation properties,<sup>26</sup> which are conducive for achieving efficient charge transport. Indeed, DPP-based conjugated polymers have achieved high performance in organic thermoelectrics and OFETs.<sup>19,27–29</sup> In P29DPP-BT and P29DPP-BTOM, a long-branched alkyl side chain with an extended branching position (six carbons between the branching point and backbone) was introduced at both sides of the N atom of the DPP; our previous reports have shown that such an alkyl side chain can result in a high charge-carrier mobility due to increased intermolecular interactions with short  $\pi$ - $\pi$  stacking distances, without compromising the solubility of the DPP-based polymers.<sup>29</sup> The DPP unit with long-branched alkyl side chains, combined with the sufficient intramolecular alkyl chain distance provided by the presence of the BT unit in the backbone, were expected to produce vacancies in the side chain regions of the polymer films, which would enhance the doping efficiency by enabling the efficient penetration of dopant molecules in the vicinity of the polymer backbone.<sup>30–32</sup>

Polymer P29DPP-BT has no functional groups at the BT units, whereas P29DPP-BTOM has methoxy groups at its BT units. Density functional theory (DFT) calculations were performed to elucidate the effect of methoxy substitution on the conformation and electronic structure of the polymers (Figures 1B,C and S9). For calculation

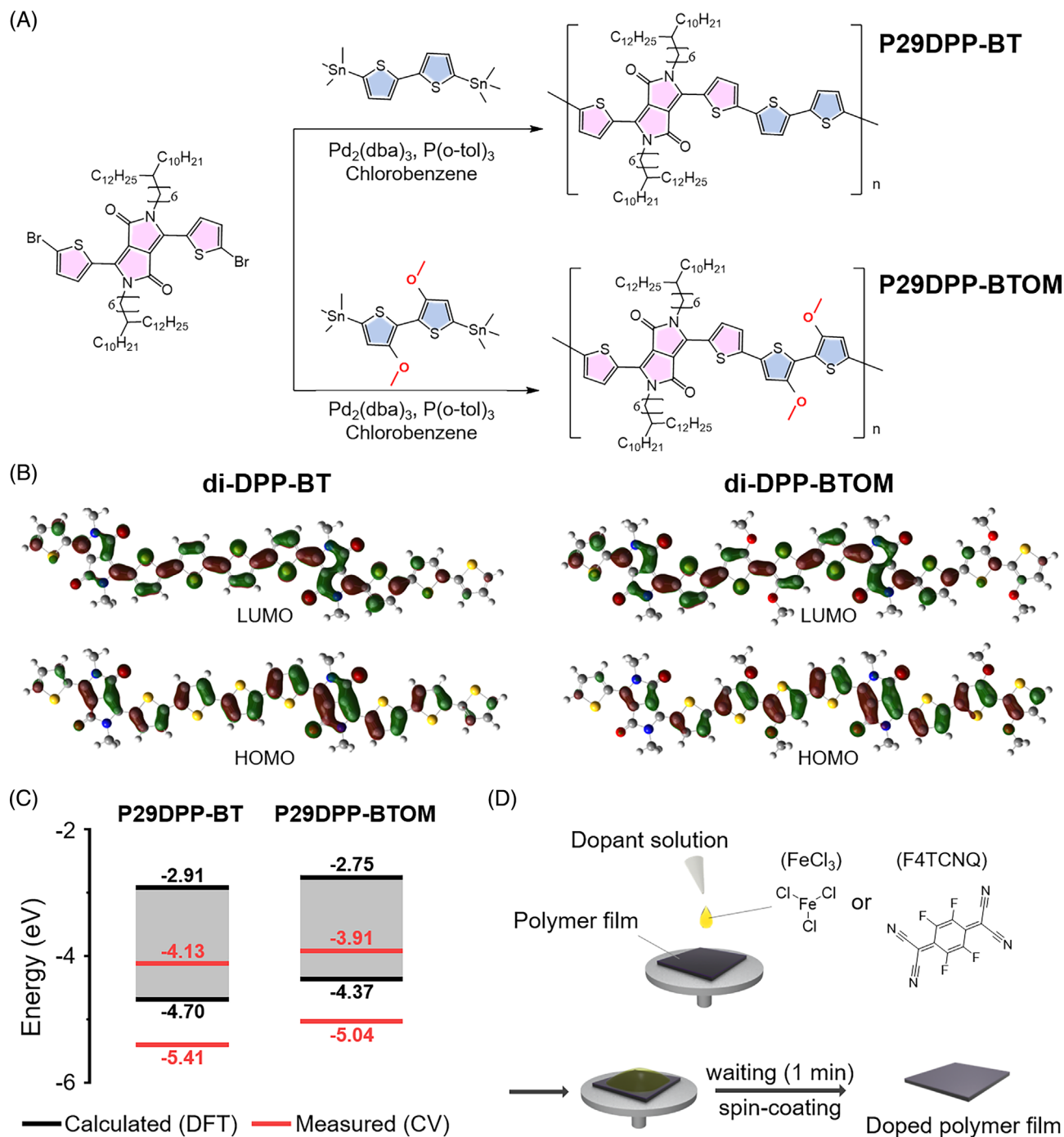


**FIGURE 1** (A) Schematic of the synthesis of P29DPP-BT and P29DPP-BTOM. (B) DFT calculation of the spatial distribution of the HOMO and LUMO of the dimers. (C) Calculated and measured HOMO and LUMO energy levels of P29DPP-BT and P29DPP-BTOM. (D) Schematic of the solution sequential doping process and structure of dopants used in this study.

simplicity, the dimers, di-DPP-BT and di-DPP-BTOM, were used, and the long-branched alkyl side chains were replaced with the methyl groups. An energy-minimized conformation showed the high planarity of the conjugated backbone of both the dimers, but di-DPP-BTOM had improved planarity compared to the di-DPP-BT; the dihedral angles between the BT (or BTOM)

unit and thiophene-flanked DPP unit ( $\theta_1$ ) and between the two thiophenes in the BT unit ( $\theta_2$ ) were  $\theta_1 = 6.37^\circ$  and  $\theta_2 = 6.75^\circ$  for di-DPP-BT, and  $\theta_1 = 2.14^\circ$  and  $\theta_2 = 1.37^\circ$  for di-DPP-BTOM. The improved planarity of di-DPP-BTOM is attributed to the intramolecular non-covalent S(thienyl)⋯O(alkoxy) interactions which enables the self-planarized conformation of the BTOM

TABLE 1 Physical properties of the DPP-based polymers.

Polymer	$M_n$ (kDa)/PDI	$T_d$ (°C)	$E_{\text{HOMO}}^a$ (eV)	$E_{\text{LUMO}}^a$ (eV)	$E_{g,\text{calc}}^a$ (eV)	$E_{\text{HOMO}}^b$ (eV)	$E_{\text{LUMO}}^b$ (eV)	$E_{g,\text{opt}}^c$ (eV)
P29DPP-BT	23/3.28	404	-4.70	-2.91	1.79	-5.41	-4.13	1.28
P29DPP-BTOM	44/7.67	364	-4.37	-2.75	1.62	-5.04	-3.91	1.13

<sup>a</sup>From DFT calculations.

<sup>b</sup> $E_{\text{HOMO}}$  from the onset potentials versus Fc/Fc<sup>+</sup> as the external reference in the CV measurements, and  $E_{\text{LUMO}} = E_{\text{HOMO}} + E_g^{\text{opt}}$ .

<sup>c</sup>From the absorption onset of the UV-vis-NIR spectra.

unit.<sup>9</sup> The calculated potential energy surfaces of the dimers obtained for different  $\theta_2$  values showed a much higher torsional barrier for di-DPP-BTOM than for di-DPP-BT (Figure S9), further supporting the enhanced backbone planarity of di-DPP-BTOM due to the introduction of the methoxy group. The calculated highest occupied molecular orbital (HOMO) and lowest unoccupied molecular orbital (LUMO) wave functions were delocalized over the dimers (Figure 1B). The presence of electron-donating methoxy groups in di-DPP-BTOM increased the HOMO and LUMO energy levels of di-DPP-BTOM compared to those of di-DPP-BT. Additionally, this modification resulted in a decreased energy gap between the HOMO and LUMO levels of di-DPP-BTOM compared to di-DPP-BT. This trend agreed well with the experimentally determined HOMO and LUMO energy levels of P29DPP-BT and P29DPP-BTOM using cyclic voltammetry (Figures 1C and S10). The higher HOMO energy level of P29DPP-BTOM compared to that of P29DPP-BT was expected to provide P29DPP-BTOM with a greater energetic driving force for electron transfer to the dopants.

Each polymer was doped with either 2,3,5,6-tetrafluoro-7,7,8,8-tetracyanoquinodimethane (F4TCNQ) or FeCl<sub>3</sub> using the solution sequential doping method in which the dopant solution was overcoated onto the prepared polymer films (Figure 1D) to compare the doping behavior and thermoelectric characteristics of the polymers. F4TCNQ and FeCl<sub>3</sub> are representative dopants that are most frequently used for the p-doping of conjugated polymers; however, they often exhibit different dopant strengths depending on the host polymer and doping method because of their different molecular and electronic structures.<sup>4,33–38</sup> Therefore, a comparative study of P29DPP-BT and P29DPP-BTOM using these two dopants is expected to provide useful insights into the effect of the methoxy functionalization on the doping behavior of the polymers. For the preparation of doped polymer thin films, the dopant solution was dropped entirely onto the polymer films and maintained for a minute to provide sufficient time for the diffusion of the dopants into the polymer film. The concentration of the dopant solution was adjusted to control the amount of the dopant residing in the doped polymer films.

To investigate the doping behavior of the polymers, a series of spectroscopic analyses were performed. Ultraviolet-visible-near-infrared (UV-vis-NIR) absorption spectra were recorded for neat and doped polymer films (Figure 2A). The spectra of the neat polymer films showed the effect of methoxy substitution on the optical bandgap and aggregation state of the neat polymer. The presence of the methoxy groups on the BT unit resulted in a decreased optical bandgap in P29DPP-BTOM compared to that in P29DPP-BT. This observation is consistent with the DFT calculation and cyclic voltammetry results; the optical band gaps ( $E_{g,\text{opt}}$ s) of the polymers calculated from the absorption edges were 1.28 and 1.11 eV for P29DPP-BT and P29DPP-BTOM, respectively. Both polymers exhibit intramolecular charge transfer (ICT) absorption, which is typically observed in D-A type conjugated polymers. The ICT absorption peaked at 1.57 and 1.37 eV for P29DPP-BT and P29DPP-BTOM, respectively. The absorption shoulder at 1.74 eV observed in neat P29DPP-BT but not in neat P29DPP-BTOM, indicated that P29DPP-BT had a stronger tendency to form aggregates in the solid state than P29DPP-BTOM. Further details on the aggregation and molecular packing structures of the polymers are discussed later. In the absorption spectra of the doped polymer films (with 2 mg mL<sup>-1</sup> dopant solution), significant differences were found depending on the dopant; FeCl<sub>3</sub> doping led to a decrease in the absorption of the neat polymer and the appearance of doping-induced broad polaronic peaks at 0.8–1.0 eV (intermediate-energy peak) and <0.5 eV (low-energy peak) for both P29DPP-BT and P29DPP-BTOM; however, F4TCNQ doping led to a similar change for P29DPP-BTOM and small change (merely a slight decrease in the neat film absorption) in the absorption spectrum of P29DPP-BT. The peaks at 1.41 and 1.60 eV in the F4TCNQ-doped P29DPP-BTOM are attributed to the absorption of the F4TCNQ anion.<sup>39</sup> These results suggest that FeCl<sub>3</sub> is an effective dopant for both polymers, while F4TCNQ can dope only P29DPP-BTOM and cannot act as a dopant for P29DPP-BT.

Electron spin resonance (ESR) measurements were performed to further characterize the doping behavior

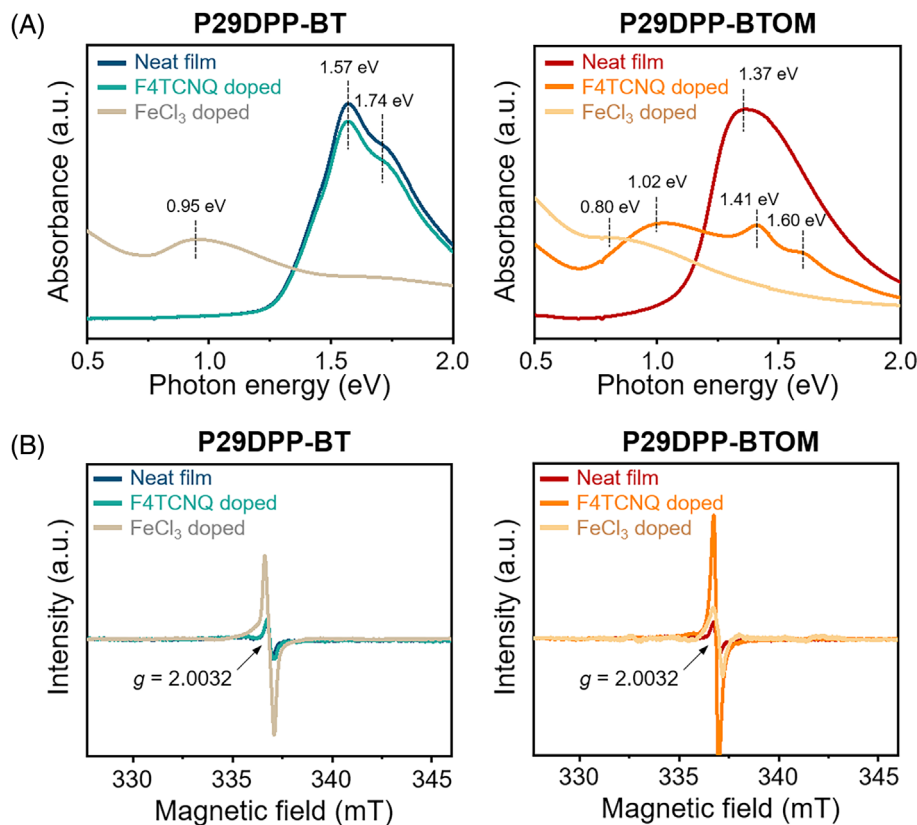
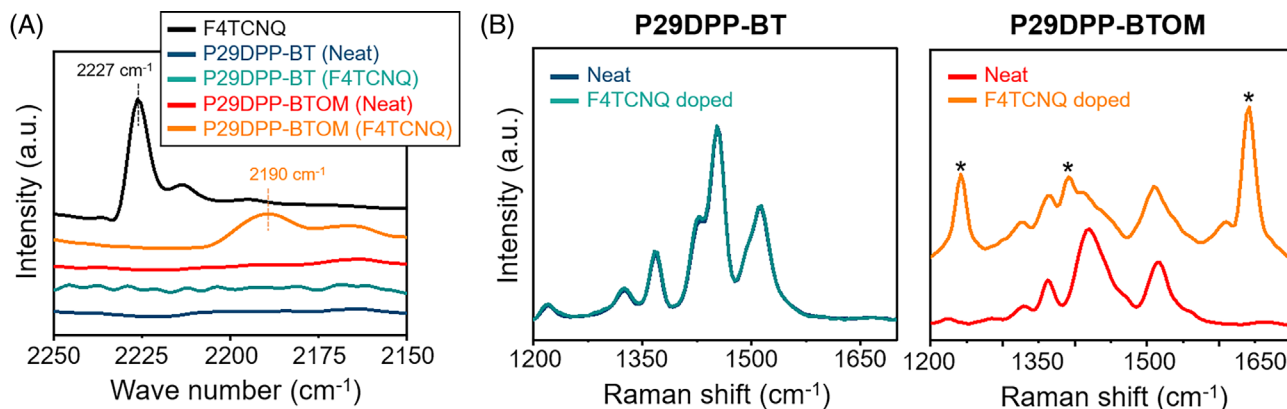


FIGURE 2 (A) UV-vis-NIR spectra of neat (undoped) and doped polymer films. (B) ESR spectra of neat (undoped) and doped polymer films. Left: P29DPP-BT. Right: P29DPP-BTOM.

(Figure 2B). The doped polymer samples for ESR measurements were prepared in the same manner as those for the UV-vis-NIR measurements. As the ESR signal arises from unpaired electrons, ESR measurements can be used to detect polarons generated by doping. However, it should be noted that the intensity of the ESR signals does not directly reflect the doping level because polaron pairs and bipolarons, which tend to be formed under high doping levels, have no spin and are not detected in ESR measurements. In the case of  $\text{FeCl}_3$  doping of P29DPP-BT and P29DPP-BTOM, the ESR intensity of the doped polymer films increased compared to that of the neat polymer films, indicating doping-induced formation of polarons. In the case of F4TCNQ doping, an increase in the ESR intensity compared to that of the neat polymer film was observed only for the doped P29DPP-BTOM, indicating that F4TCNQ can be used to dope only P29DPP-BTOM and not P29DPP-BT. This result is consistent with our UV-vis-NIR measurements.

The ability of the dopants to generate charge carriers within P29DPP-BT and P29DPP-BTOM was estimated from the UV-vis-NIR and ESR results (Figure 2). In general, polaronic absorption peaks at intermediate and low energies develop as the doping level increases. As the doping level increases further, the absorption of the intermediate-energy peak reaches a maximum and then decreases again, while the absorption of the low-energy

peak continuously increases and becomes dominant,<sup>40</sup> because the transition from single polarons to polaron pairs and bipolarons occurs at high doping levels.<sup>41</sup> In the comparison of the absorption spectra of  $\text{FeCl}_3$ - and F4TCNQ-doped P29DPP-BTOM films, the absorbance of the low-energy polaronic peak was higher, and the absorbance of the intermediate-energy polaronic peak was lower in the  $\text{FeCl}_3$ -doped film than in the F4TCNQ-doped film, indicating that more charge carriers were generated in the  $\text{FeCl}_3$ -doped film than in the F4TCNQ-doped film. The intensity ratio of the polaronic absorption peak (e.g., the absorption at 0.5 eV) to the neutral  $\pi$ - $\pi^*$  absorption peak is higher in the  $\text{FeCl}_3$ -doped P29DPP-BTOM (2.89) than in the  $\text{FeCl}_3$ -doped P29DPP-BT (2.09), indicating that more charge carriers are generated in  $\text{FeCl}_3$ -doped P29DPP-BTOM. In the ESR measurements, the signal intensity was highest for F4TCNQ-doped P29DPP-BTOM, followed by  $\text{FeCl}_3$ -doped P29DPP-BT, and  $\text{FeCl}_3$ -doped P29DPP-BTOM. This trend is the result of the formation of spinless polaron pairs and bipolarons at high doping levels; that is,  $\text{FeCl}_3$ -doped P29DPP-BT and  $\text{FeCl}_3$ -doped P29DPP-BTOM have higher doping levels than F4TCNQ-doped P29DPP-BTOM, but their ESR intensities are weaker because a significant fraction of the polarons is converted into polaron pairs and/or bipolarons. The weaker ESR signal of  $\text{FeCl}_3$ -doped P29DPP-BTOM compared to that



**FIGURE 3** (A) FTIR spectra of neat (undoped) and F4TCNQ-doped polymer films (the spectrum of pure F4TCNQ is also shown). (B) Raman spectra of neat (undoped) and F4TCNQ-doped polymer films. Left: P29DPP-BT. Right: P29DPP-BTOM. The asterisks indicate the peaks from F4TCNQ anion.

of  $\text{FeCl}_3$ -doped P29DPP-BT can be understood in the same way, although the exact quantification of each polaronic species is challenging at this stage. The charge-carrier concentrations of the doped polymer films are further discussed quantitatively later.

The most important difference between the doping behaviors of the two polymers is that F4TCNQ can dope only P29DPP-BTOM and not P29DPP-BT. To further elucidate the doping behavior of the polymers upon F4TCNQ doping, Fourier-Transform infrared (FTIR) spectra were obtained (Figure 3A). Upon doping, the charge transfer from polymer to F4TCNQ leads to the negatively charged state of F4TCNQ, which shifts the vibrational frequency of the cyano-group compared to that of neutral F4TCNQ; the cyano-vibrational frequency of neutral and anion state of F4TCNQ is  $\sim 2227$  and  $2192 \text{ cm}^{-1}$ , respectively.<sup>39,42</sup> In the FTIR spectrum of F4TCNQ-doped P29DPP-BTOM, a cyano-vibrational peak appeared at  $\sim 2190 \text{ cm}^{-1}$ , indicating integer charge transfer between P29DPP-BTOM and F4TCNQ. However, no cyano-vibrational peaks were observed in the FTIR spectrum of F4TCNQ-doped P29DPP-BT, although the sample was prepared using the same F4TCNQ doping process as in P29DPP-BTOM. The absence of a cyano-vibration peak indicates that a negligible amount of F4TCNQ penetrated the P29DPP-BT film during the doping process. Raman spectrum also supports the absence of F4TCNQ in the F4TCNQ-doped P29DPP-BT film (Figure 3B). P29DPP-BTOM exhibited significant changes in the vibronic transition peaks before and after doping with F4TCNQ, indicating a change in the vibronic transition mode of the polymer upon doping. In addition, the peaks at  $1242$ ,  $1390$ , and  $1641 \text{ cm}^{-1}$ , which correspond to the vibronic transition peaks of the F4TCNQ anion,<sup>43</sup> were clearly observed after doping. In contrast, the Raman spectrum of P29DPP-BT showed little change

after doping with F4TCNQ, indicating that charge transfer did not occur between P29DPP-BT and F4TCNQ. In addition, vibronic transition peaks of the neutral or anionic F4TCNQ were not observed, indicating that F4TCNQ was not incorporated into the P29DPP-BT film even after the doping process. Based on these results, the lack of polaronic features of F4TCNQ-doped P29DPP-BT in the UV-vis-NIR and ESR measurements can be attributed to the limited penetration of F4TCNQ into the polymer film.

To investigate the structural origin of the selective doping capability of F4TCNQ, two-dimensional grazing incidence x-ray diffraction (2D GIXD) measurements were performed on the polymer films, and their microstructures and molecular ordering were analyzed (Figure 4). The GIXD patterns of the polymer films, containing distinctive peaks of ( $h00$ ) and ( $010$ ) reflections that arise from the lamella stacking and  $\pi$ - $\pi$  stacking of the polymer chains, respectively (Figure 4A), indicate the highly crystalline structure of the polymer films. The highly crystalline film morphology can also be observed from the atomic force microscopy (AFM) images (inset of Figure 4A), in which the fibrillar structures of the polymer film surface are clearly visible. In the GIXD pattern of the P29DPP-BT film, ( $h00$ ) peaks were observed along the out-of-plane direction, whereas the ( $010$ ) peak was observed along the in-plane direction, indicating that the crystallites had a preferential edge-on orientation distribution. In contrast, the GIXD pattern of the P29DPP-BTOM film exhibited both ( $h00$ ) and ( $010$ ) peaks along the out-of-plane and in-plane directions, indicating a bimodal orientation distribution of the crystallites, that is, the coexistence of face-on and edge-on crystallites in the film. The intensities of the ( $h00$ ) and ( $010$ ) peaks were higher for the P29DPP-BT film than for the P29DPP-BTOM film. The lamellar-stacking and  $\pi$ - $\pi$

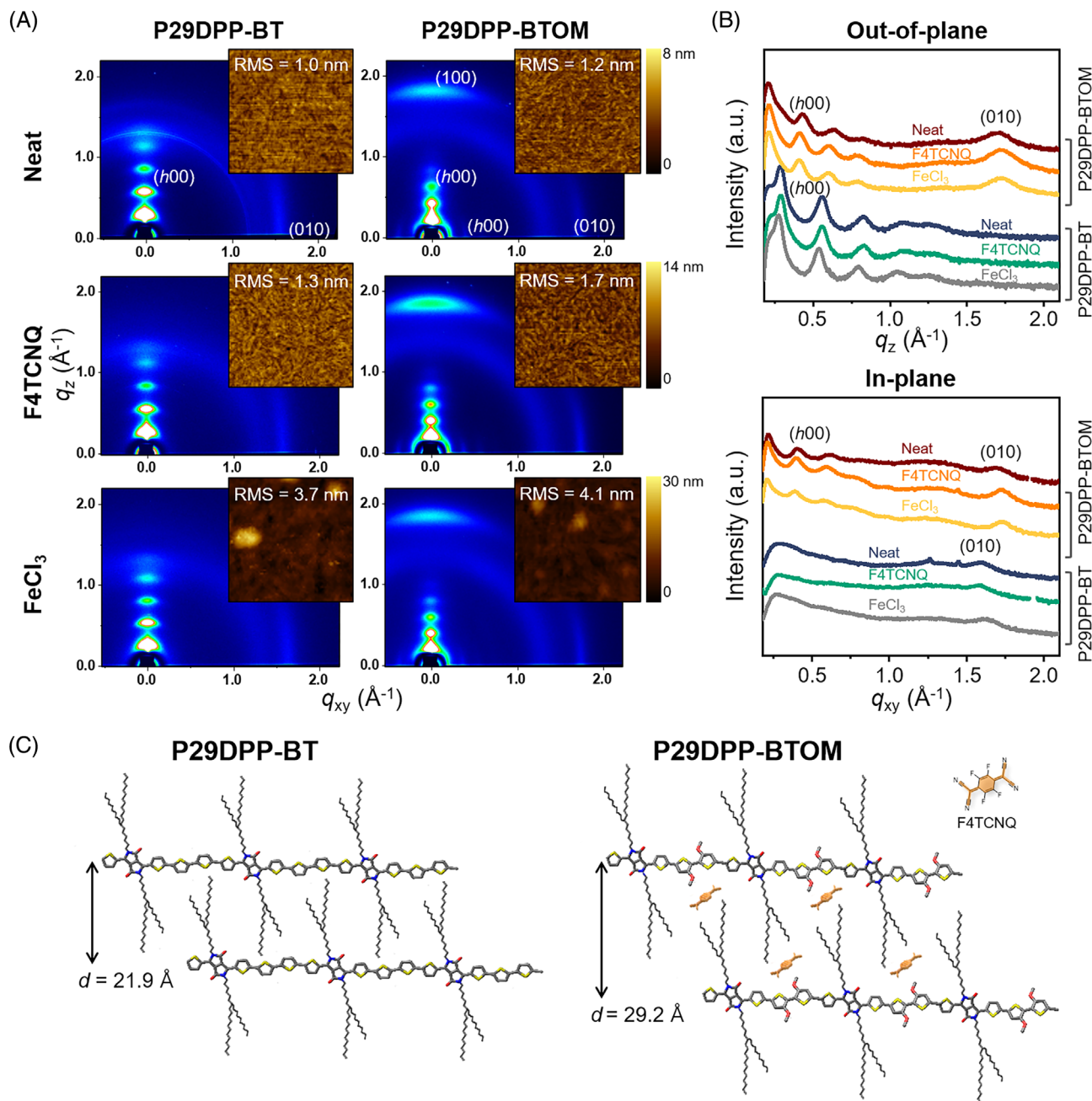


**FIGURE 4** Characterization of the crystalline structure of neat and doped polymer films. (A) 2D GIXD patterns and AFM height images (inset,  $2 \mu\text{m} \times 2 \mu\text{m}$ ). Root-mean-square (RMS) roughness is also given in the AFM images. (B) 1D profiles for the 2D GIXD patterns along the out-of-plane (top) and in-plane (bottom) directions. (C) Schematic representation of the lamellar packing structure of the polymers.

stacking distances were also evaluated from the one-dimensional (1D) plots of the diffraction patterns along the out-of-plane and in-plane directions (Figure 4B). The detailed results of the structural analysis including the peak positions,  $d$ -spacing, full-width at half maximum (FWHM), coherence lengths, and paracrystalline disorder parameters ( $g$ ) are listed in Table 2.

In the case of neat polymers, the lamellar spacing is much larger in the P29DPP-BTOM ( $29.2$  Å) than in the P29DPP-BT ( $21.9$  Å), while the  $\pi$ - $\pi$  stacking distance is

smaller in the P29DPP-BTOM ( $3.68$  Å) than in the P29DPP-BT ( $3.93$  Å). The larger lamellar spacing of P29DPP-BTOM is attributed to the presence of the methoxy group, which interrupted the close interdigitation of the alkyl side chains during lamellar stacking. The smaller  $\pi$ - $\pi$  stacking distance of P29DPP-BTOM is attributed to the improved planarity of the polymer backbone of P29DPP-BTOM compared to the polymer backbone of P29DPP-BT that arises from the incorporation of methoxy group, as confirmed by our DFT calculations. Upon



TABLE 2 Detailed information of crystalline structure of neat (undoped) and doped polymer films.

Crystallographic parameters		P29DPP-BT			P29DPP-BTOM		
		Neat	F4TCNQ	FeCl <sub>3</sub>	Neat	F4TCNQ	FeCl <sub>3</sub>
Lamellar stacking (100)	$q$ (Å <sup>-1</sup> )	0.287	0.289	0.275	0.215	0.206	0.205
	$d$ -spacing (Å)	21.89	21.73	22.84	29.22	30.52	30.64
	FWHM (Å <sup>-1</sup> )	0.035	0.036	0.031	0.033	0.031	0.032
	Coherence length (Å)	160.8	155.3	185.3	171.9	181.2	176.7
	$g^a$ (%)	4.8	4.3	4.6	7.8	6.2	6.3
$\pi$ - $\pi$ stacking (010)	$q$ (Å <sup>-1</sup> )	1.597	1.591	1.628	1.706	1.730	1.731
	$d$ -spacing (Å)	3.93	3.95	3.86	3.68	3.63	3.63
	FWHM (Å <sup>-1</sup> )	0.117	0.133	0.167	0.122	0.111	0.111
	Coherence length (Å)	48.2	42.4	33.8	46.3	50.8	50.9

<sup>a</sup>The paracrystalline disorder parameter,  $g$ , was determined by the equation,  $m = g^2\pi^2/d$ , where  $m$  is the slope of  $\delta b-h^2$  plot,  $\delta b$  is the integral width of the diffraction peaks,  $h$  is the order of the diffraction, and  $d$  is the lamellar stacking distance.

FeCl<sub>3</sub> doping, the lamellar stacking distances were slightly increased (by  $\sim 1.0$ – $1.4$  Å) and  $\pi$ - $\pi$  stacking distances were slightly decreased (by  $\sim 0.05$ – $0.07$  Å) for both P29DPP-BT and P29DPP-BTOM. It is likely that the small size of FeCl<sub>3</sub> allowed FeCl<sub>3</sub> to be effectively incorporated into the crystal structure of the polymers. Upon F4TCNQ doping, P29DPP-BTOM exhibited the changes in its crystalline structure resembling those observed with FeCl<sub>3</sub> doping. Specifically, there was an increase in the lamellar stacking distance by  $\sim 1.3$  Å and a slight decrease in the  $\pi$ - $\pi$  stacking distance by  $\sim 0.05$  Å. Conversely, P29DPP-BT did not exhibit significant changes in its crystalline structure and maintained a structure that closely resembled that of the neat P29DPP-BT film. The slight change in the GIXD pattern of F4TCNQ-doped P29DPP-BT is consistent with our earlier spectroscopic observations (i.e., UN-vis-NIR absorption, ESR, FTIR, and Raman spectra) that F4TCNQ cannot be incorporated into the P29DPP-BT film through the sequential doping process.

F4TCNQ could not be incorporated into the P29DPP-BT film because of the tight lamellar packing of its side chains. This tight arrangement did not provide enough space for F4TCNQ to reside within the crystalline structure of P29DPP-BT, because of the larger size of the F4TCNQ molecule compared to that of FeCl<sub>3</sub>. Unlike P29DPP-BT, P29DPP-BTOM can include F4TCNQ within its crystalline structure because of the larger lamellar stacking distance of P29DPP-BTOM compared with that of P29DPP-BT. Consequently, F4TCNQ can be effectively incorporated into the crystalline matrix of P29DPP-BTOM due to the availability of a volume between the alkyl side chains. This explanation is schematically illustrated in Figure 4C. It has been widely reported that for F4TCNQ-doped conjugated polymers, F4TCNQ is preferentially located within the

crystalline phase of the polymer film rather than in the amorphous phase,<sup>44–46</sup> implying that the diffusion of F4TCNQ within the crystalline phase has a critical impact on the doping kinetics of the polymers. In addition, previous reports have demonstrated that a dopant can have comparable diffusion coefficients in the crystalline and amorphous phases of a conjugated polymer film,<sup>46</sup> and that a conjugated polymer film with high crystallinity can even have a larger diffusion coefficient for a dopant molecule within the film than a film with lower crystallinity.<sup>47</sup> Therefore, the inability of F4TCNQ to enter the crystalline structure of P29DPP-BT is considered to be the primary reason why F4TCNQ could not penetrate the P29DPP-BT film and thus could not dope the polymer.

To further elucidate the possible chemical origin of the selective doping capability of F4TCNQ, we investigated the interaction of F4TCNQ with P29DPP-BT and P29DPP-BTOM using DFT calculations. In the calculations, an F4TCNQ molecule was placed in the proximity of di-DPP-BT or di-DPP-BTOM, and the total energies were calculated for various angles and intermolecular distances to determine the structure with the minimal energy (Figure S11). The total energy was set to zero when the intermolecular distance was sufficiently large to prevent any interaction between the molecules. The minimized energies of the two F4TCNQ-dimer complexes were negative for both dimers, indicating a favorable interaction between F4TCNQ and the dimer molecule. The minimized energy was lower in the F4TCNQ–di-DPP-BTOM complex ( $-5.0$  kJ mol<sup>-1</sup>) than in the F4TCNQ–di-DPP-BT complex ( $-1.6$  kJ mol<sup>-1</sup>), indicating that the presence of methoxy groups renders the approach of F4TCNQ molecule to the polymer backbone energetically more favorable.

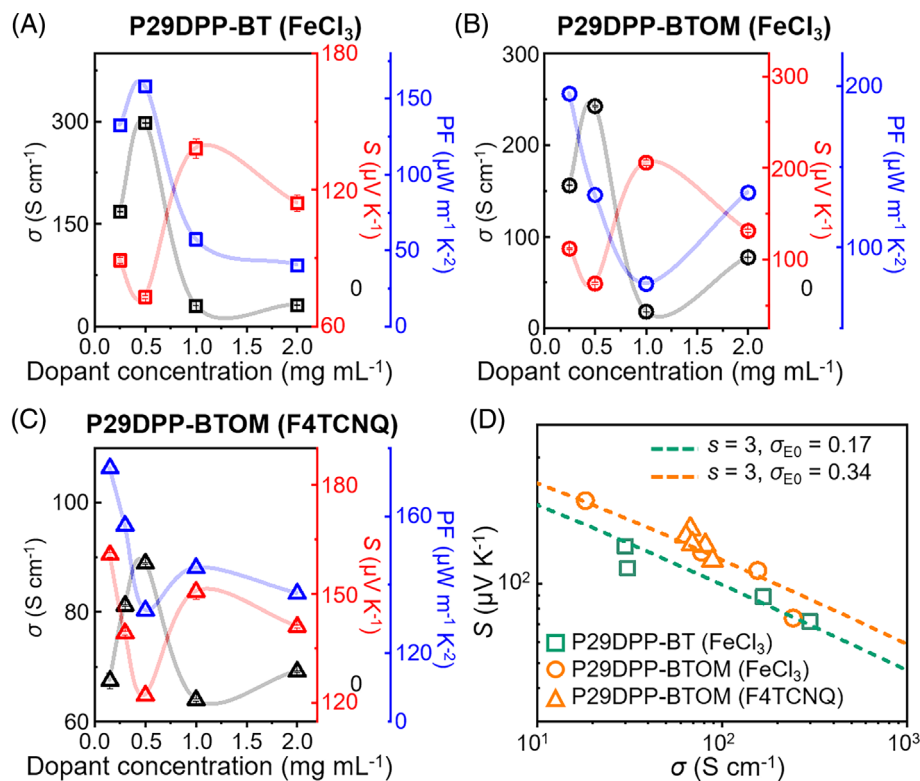


**FIGURE 5** Thermoelectric properties of the doped polymers. (a–c)  $\sigma$  (black symbols),  $S$  (red symbols), and  $PF$  (blue symbols) of the doped polymers as functions of dopant concentration. (d)  $S$ - $\sigma$  plot of doped polymers. Symbols: measured data points. Dashed lines: Fitted curves by Kang-Snyder charge transport model ( $s = 3$ ).

The effects of the methoxy functionalization on charge transport and thermoelectric properties of the polymers were investigated by measuring the charge-carrier mobility,  $\sigma$ , and  $S$  of neat and doped P29DPP-BT and P29DPP-BTOM films. The charge-carrier mobilities of the neat polymers were measured by fabricating OFETs (Figures S12 and S13 and Table S1). The devices were fabricated by depositing polymer films onto octadecyltrimethoxysilane (OTS)-treated SiO<sub>2</sub> (300 nm)/Si substrates, followed by the thermal evaporation of Au electrodes onto the polymer films. The details of the device fabrication method are provided in the Experimental Section. P29DPP-BT exhibited the highest field-effect hole mobility ( $\mu_{h,FET}$ ) of 0.35 ( $\pm 0.05$ ) cm<sup>2</sup> V<sup>-1</sup> s<sup>-1</sup> at the optimal thermal annealing temperature of 200°C.  $\mu_{h,FET}$  of P29DPP-BT at different thermal annealing temperatures was not much different from the optimal value. P29DPP-BTOM showed significantly lower  $\mu_{h,FET}$  values, approximately one order of magnitude lower than P29DPP-BT. The highest  $\mu_{h,FET}$  value recorded for P29DPP-BTOM was 0.017 ( $\pm 0.001$ ) cm<sup>2</sup> V<sup>-1</sup> s<sup>-1</sup> at the optimal thermal annealing temperature of 200°C. The thermal annealing temperature did not cause a significant change in the  $\mu_{h,FET}$ s of the P29DPP-BTOM FET. In the temperature-dependent measurement of  $\mu_{h,FET}$  of the neat polymers,  $\mu_{h,FET}$  increased with the increasing temperature, indicating hopping transport of holes within the polymer films (Figure S14). The lower  $\mu_{h,FET}$  of P29DPP-BTOM than P29DPP-BT, despite its higher

backbone planarity and shorter  $\pi$ - $\pi$  stacking distance, can be attributed mainly to the bimodal orientation distribution of P29DPP-BTOM crystals; this bimodal distribution is less favorable for in-plane charge transport compared to the edge-on dominant orientation distribution of the P29DPP-BT.<sup>12,48</sup> The high degree of paracrystalline disorder in P29DPP-BTOM compared to that in P29DPP-BT could also contribute to the lower  $\mu_{h,FET}$  of P29DPP-BTOM (Figure 4 and Table 2). Our previous study has already reported an order of magnitude lower charge-carrier mobility in a backbone-methoxy functionalized conjugated polymer compared to its non-methoxy functionalized counterpart; the  $\mu_{h,FET}$  of P29DPP-BT and P29DPP-BTOM in the present work follows a trend similar to that in our previous work.<sup>12</sup>

In the case of FeCl<sub>3</sub> doping, the  $\sigma$  values of P29DPP-BT and P29DPP-BTOM increased with the concentration of the dopant solution at low concentrations but decreased again at higher concentrations (Figure 5 and Table 3). The maximum  $\sigma$  values were 298 and 242.4 S cm<sup>-1</sup> for P29DPP-BT and P29DPP-BTOM, respectively. Although the neat P29DPP-BTOM has an order of magnitude lower charge-carrier mobility than neat P29DPP-BT, the  $\sigma$  of FeCl<sub>3</sub>-doped P29DPP-BTOM is comparable to that of FeCl<sub>3</sub>-doped P29DPP-BT at a given dopant concentration. This result, together with the stronger polaronic absorption intensity of FeCl<sub>3</sub>-doped P29DPP-BTOM than that of FeCl<sub>3</sub>-doped P29DPP-BT under the same FeCl<sub>3</sub> doping conditions shown in the

TABLE 3 Thermoelectric properties of doped polymers.

Polymer	Dopant	Dopant concentration (mg mL <sup>-1</sup> )	Electrical Conductivity (S cm <sup>-1</sup> )	Seebeck coefficient (μV K <sup>-1</sup> )	Power factor (μW m <sup>-1</sup> K <sup>-2</sup> )
P29DPP-BT	FeCl <sub>3</sub>	0.25	167.5 ± 0.5	89.0 ± 1.5	132.7
		0.5	298 ± 0.3	72.9 ± 0.6	158.4
		1	30.0 ± 0.1	138.2 ± 4.3	57.30
		2	30.9 ± 0.2	114.1 ± 3.7	40.23
P29DPP-BTOM	FeCl <sub>3</sub>	0.25	155.8 ± 0.5	111.9 ± 1.1	195.1
		0.5	242.4 ± 0.5	73.9 ± 1.3	132.4
		1	18.3 ± 0.1	205.8 ± 3.1	77.51
		2	77.5 ± 0.1	131.4 ± 1.8	133.8
	F4TCNQ	0.15	67.4 ± 1.4	160.7 ± 0.6	174.1
		0.3	81.2 ± 0.1	139.2 ± 0.6	157.3
		0.5	88.9 ± 0.1	122.1 ± 1.6	132.5
		1	63.9 ± 0.2	150.6 ± 2.1	144.9
		2	69.1 ± 0.1	141 ± 0.5	137.4

UV-vis-NIR absorption spectra (Figure 2A), indicates that FeCl<sub>3</sub>-doped P29DPP-BTOM has a higher doping efficiency, and thus, a higher charge carrier concentration than FeCl<sub>3</sub>-doped P29DPP-BT. Furthermore, the higher charge carrier concentration of doped P29DPP-BTOM was also confirmed by an AC Hall-effect measurement, which exhibited approximately an order of magnitude higher charge carrier concentration in FeCl<sub>3</sub>-doped P29DPP-BTOM ( $n_{\text{Hall}} = 5.73 \times 10^{21} \text{ cm}^{-3}$ ) than that in FeCl<sub>3</sub>-doped P29DPP-BT ( $n_{\text{Hall}} = 2.12 \times 10^{20} \text{ cm}^{-3}$ ) at the optimal doping concentrations. The improved doping efficiency of P29DPP-BTOM upon FeCl<sub>3</sub> doping can be attributed to the increased lamellar spacing of P29DPP-BTOM due to the introduction of methoxy groups (Table 2), which provides a low energy barrier for dopant diffusion within the polymer film during the doping process.<sup>49</sup>

A high doping efficiency and concomitant high charge carrier concentration can result in an improved charge-carrier mobility in a doped polymer film compared to that in an undoped polymer film, because the trap states of the polymer film are filled at high charge carrier concentrations and charge transport becomes more efficient due to the reduced trap density.<sup>48</sup> The same would happen in the FeCl<sub>3</sub>-doped P29DPP-BTOM; that is, the high doping efficiency of P29DPP-BTOM can lead to a significant increase in the charge-carrier mobility of doped P29DPP-BTOM compared to that of neat P29DPP-BTOM, which would contribute to the comparable electrical conductivities of FeCl<sub>3</sub>-doped P29DPP-BTOM and P29DPP-BT. Indeed, the AC Hall-effect measurements indicated a greater increase in the charge-carrier mobility upon doping for FeCl<sub>3</sub>-doped

P29DPP-BTOM than for FeCl<sub>3</sub>-doped P29DPP-BT. The measured charge-carrier mobility ( $\mu_{\text{Hall}}$ ) for FeCl<sub>3</sub>-doped P29DPP-BTOM was  $0.18 \text{ cm}^2 \text{ V}^{-1} \text{ s}^{-1}$ , which corresponds to an approximately 11-fold increase compared to  $\mu_{\text{h,FET}}$  of the neat polymer. For FeCl<sub>3</sub>-doped P29DPP-BT, the measured  $\mu_{\text{Hall}}$  was found to be  $2.44 \text{ cm}^2 \text{ V}^{-1} \text{ s}^{-1}$ , representing approximately 7-fold increase compared to the  $\mu_{\text{h,FET}}$  of the neat polymer. These results support our speculation. When measuring the temperature dependence of the electrical conductivities of FeCl<sub>3</sub>-doped P29DPP-BT and P29DPP-BTOM (Figure S15), a smaller activation energy ( $E_a$ ) was obtained for charge conduction in P29DPP-BTOM (13.7 meV) than that in P29DPP-BT (20.8 meV), which further supports more efficient charge transport in FeCl<sub>3</sub>-doped P29DPP-BTOM than in FeCl<sub>3</sub>-doped P29DPP-BT.

In the case of F4TCNQ doping, only P29DPP-BTOM could be doped by F4TCNQ, resulting in a maximum  $\sigma$  of  $88.9 \text{ S cm}^{-1}$ , which is lower than the maximum  $\sigma$  of FeCl<sub>3</sub>-doped P29DPP-BTOM. The crystalline structure of the F4TCNQ-doped P29DPP-BTOM film was nearly identical to that of the FeCl<sub>3</sub>-doped film (Table 2), suggesting that the different molecular sizes and structures of F4TCNQ and FeCl<sub>3</sub> did not cause considerable microstructural differences between the F4TCNQ-doped and FeCl<sub>3</sub>-doped P29DPP-BTOM films. This similarity can be attributed to the wide lamellar spacing and ample space between the alkyl side chains, which provide sufficient room for the accommodation of the dopant molecules. Therefore, the smaller maximum  $\sigma$  of F4TCNQ-doped film is primarily attributed to the weaker oxidation strength of F4TCNQ compared to FeCl<sub>3</sub>, rather than the

structural difference between the F4TCNQ-doped and FeCl<sub>3</sub>-doped P29DPP-BTOM films. The lower doping efficiency of the F4TCNQ than FeCl<sub>3</sub> is supported by the weaker polaronic absorption peaks of F4TCNQ-doped P29DPP-BTOM film compared to that of the FeCl<sub>3</sub>-doped film (Figure 2A). Additionally, the lower charge carrier concentration measured by AC Hall-effect measurements of F4TCNQ-doped P29DPP-BTOM film ( $n_{\text{Hall}} = 1.95 \times 10^{21} \text{ cm}^{-3}$  and  $\mu_{\text{Hall}} = 0.18 \text{ cm}^2 \text{ V}^{-1} \text{ s}^{-1}$ ) compared to the FeCl<sub>3</sub>-doped P29DPP-BTOM film ( $n_{\text{Hall}} = 5.73 \times 10^{21} \text{ cm}^{-3}$  and  $\mu_{\text{Hall}} = 0.18 \text{ cm}^2 \text{ V}^{-1} \text{ s}^{-1}$ ), further confirms the lower doping efficiency of F4TCNQ. The  $E_a$  for charge carrier transport of F4TCNQ-doped P29DPP-BTOM, measured by the temperature dependence of the electrical conductivity (Figure S15), was 25.8 meV, which is about two times larger than that of FeCl<sub>3</sub>-doped P29DPP-BTOM. Note that this trend agrees well with a previous report that the higher the room-temperature electrical conductivity, the lower the  $E_a$ .<sup>50</sup> The higher activation energy observed in the F4TCNQ-doped film compared to the FeCl<sub>3</sub>-doped film is attributed to the lower charge-carrier concentration in the F4TCNQ-doped film; the lower charge-carrier concentration results in less filling of the trap states within the material, leading to a higher activation energy for charge transport.

Finally, the Seebeck coefficients of the doped polymer films were measured, and the PFs were calculated (Figure 5A–C and Table 3). The Seebeck coefficient was determined from the linear slope between the thermovoltage and temperature difference between the two electrodes. The measured Seebeck coefficient tended to decrease with increasing electrical conductivity, which is consistent with the trade-off relationship between the electrical conductivity and Seebeck coefficient. The  $S$ – $\sigma$  relationship of the doped polymer films was plotted and fitted using the Kang–Snyder charge-transport model with two fitting parameters  $s$  and  $\sigma_{E0}$ :<sup>51</sup>

$$\sigma = \sigma_{E0} \times sF_{s-1}(\eta), \quad (1)$$

$$S = \frac{k_B}{e} \left[ \frac{(s+1)F_s(\eta)}{sF_{s-1}(\eta)} - \eta \right], \quad (2)$$

where  $\sigma_{E0}$  is the transport coefficient,  $s$  is a parameter that is related to the charge conduction mechanism,  $F_i$  is the complete Fermi–Dirac integral,  $\eta$  is the reduced chemical potential,  $k_B$  is the Boltzmann constant, and  $e$  is the elementary charge. In general  $s = 3$  for most doped conjugated polymers, so we used this value in fitting our  $S$ – $\sigma$  results of P29DPP-BT and P29DPP-BTOM (Figure 5D). The data points of P29DPP-BTOM were well

fitted with a single curve, independent of the dopant used (i.e., FeCl<sub>3</sub> or F4TCNQ). Note that in the case of  $s = 1$ , another typical value used for the transport model of highly conductive polymers,<sup>51</sup> the model gave much poorer fitting compared to the case of  $s = 3$  (Figure S16). The obtained values for the fitting parameter  $\sigma_{E0}$  in Figure 5D were 0.17 and 0.34 S cm<sup>−1</sup> for doped P29DPP-BT and P29DPP-BTOM, respectively. This result indicates that for a given electrical conductivity, a higher  $S$  value can be obtained in doped P29DPP-BTOM than in doped P29DPP-BT. One possible cause is the bimodal molecular orientation distribution of the P29DPP-BTOM films. A recent study revealed that the bimodal molecular orientation distribution of a doped conjugated polymer film can lead to a higher  $S$  value than a film with a unimodal orientation distribution, and attributed the higher  $S$  value to the larger energy splitting between the Fermi level ( $E_F$ ) and transport level ( $E_{tr}$ ) obtained in a film with a bimodal distribution due to orientation-dependent molecular energy levels.<sup>49</sup> Similarly, the bimodal orientation distribution of the P29DPP-BTOM film induced by the methoxy groups is likely to result in a larger energy splitting between  $E_{tr}$  and  $E_F$  than in the edge-on dominant P29DPP-BT film, leading to a higher  $S$  value at a given electrical conductivity. The best PFs obtained were 158.3 and 195.1  $\mu\text{W m}^{-1} \text{ K}^{-2}$  for FeCl<sub>3</sub>-doped P29DPP-BT and FeCl<sub>3</sub>-doped P29DPP-BTOM, respectively.

Overall, our results demonstrate the effect of methoxy functionalization of the backbone of a D–A type conjugated copolymer on the doping behavior and thermoelectric properties of the polymer. Introducing methoxy groups into the backbone can significantly affect the microstructure of the conjugated polymer films, particularly the molecular packing structure and molecular orientation distribution. The presence of methoxy groups led to an increase in the lamellar spacing of the polymer crystals, which increased the volume between the side chains required to incorporate the dopant molecules. As a result, the dopants can more easily diffuse within the polymer film during the sequential doping process, yielding enhanced doping efficiency. Even a dopant that could not dope the polymer at all in the absence of a methoxy group (i.e., F4TCNQ in this study) could dope the polymer and be effectively incorporated into the polymer film when the polymer was methoxy functionalized because of the increased lamellar spacing caused by the introduction of the methoxy groups. In addition to the increase in doping efficiency, methoxy functionalization can also enhance the Seebeck coefficient of the doped polymer film by inducing a bimodal orientational distribution in the polymer and increasing the splitting between  $E_{tr}$  and  $E_F$  owing to the orientation-dependent molecular energy levels. These

results suggest that the methoxy functionalization of a conjugated polymer backbone is an effective way to control the properties of polymers and achieve high thermoelectric performance.

### 3 | CONCLUSION

In summary, we compared the doping behavior and thermoelectrical properties of DPP-based conjugated polymers, P29DPP-BT and P29DPP-BTOM, with and without methoxy groups on the BT unit of the backbone. Upon doping with  $\text{FeCl}_3$  or F4TCNQ, the doping efficiencies and thermoelectric properties of the two polymers differed significantly. Systematic analyses revealed that the difference mainly originated from structural differences between the two polymer films, particularly the lamellar stacking distance and molecular orientation distribution. The larger lamellar spacing of P29DPP-BTOM enabled more efficient dopant diffusion within the crystalline regions of the polymer, resulting in a higher doping efficiency compared to P29DPP-BT. This effect was even more pronounced when the polymers were doped with F4TCNQ, which has a larger molecular size than  $\text{FeCl}_3$ ; that is, F4TCNQ doped only P29DPP-BTOM and not P29DPP-BT. As a result, while the electrical conductivity of the both polymers could be enhanced by doping with  $\text{FeCl}_3$ , only P29DPP-BTOM exhibited increased electrical conductivity by doping with F4TCNQ. The presence of methoxy groups resulted in a bimodal molecular orientation distribution for P29DPP-BTOM, whereas P29DPP-BT exhibited an edge-on-dominant orientation. The bimodal orientation distribution of P29DPP-BTOM resulted in an increased energy splitting between the transport and Fermi levels of the doped polymer films, leading to an increased Seebeck coefficient compared to that of P29DPP-BT at a given electrical conductivity. Consequently, P29DPP-BTOM exhibited a higher optimized PF than P29DPP-BT.

These results clearly demonstrate the effects of methoxy functionalization on the thermoelectric properties and doping behavior of conjugated polymers. This study sheds light on how methoxy functionalization can be used to modulate the doping behavior and thermoelectric properties of conjugated polymers. Especially, our results on the doping of P29DPP-BT and P29DPP-BTOM by F4TCNQ show that the introduction of methoxy groups can even convert a conjugated polymer-dopant pair that cannot be doped into a dopable pair. This finding has significant implications for the further development of conjugated polymer-dopant systems with high doping efficiencies and thermoelectric performance.

## 4 | EXPERIMENTAL SECTION

### 4.1 | Materials

P29DPP-BT and P29DPP-BTOM were synthesized as described in Supporting Information. The dopant materials and processing solvents were purchased from Tokyo Chemical Industry (Japan) and used without further purification.

### 4.2 | Preparation of neat and doped polymer films

The polymers were dissolved in anhydrous chloroform at a concentration of  $7 \text{ mg mL}^{-1}$ . Glass substrates ( $1.25 \times 1.25 \text{ cm}^2$ ) were cleaned by ultrasonication with acetone, isopropyl alcohol, and DI water. The substrates were then dried and treated with UV-ozone plasma for 20 min. Polymer films were prepared by spin-coating the polymer solutions under  $\text{N}_2$  atmosphere. The thickness of the resulting polymer film was approximately 50 nm. Dopant solutions dissolved in acetonitrile were dripped onto the polymer films and left for 1 min, followed by spin-coating to remove the solution. The films were then annealed for 10 min at a mild temperature ( $\sim 100^\circ\text{C}$ ) to completely dry the doped polymer films.

### 4.3 | Fabrication of OFETs

OFET devices were fabricated on  $\text{SiO}_2/\text{Si}$  substrates. A highly doped p-Si wafer served as the gate electrode, and a 300 nm-thick thermally grown  $\text{SiO}_2$  layer served as the gate dielectric. For the surface treatment, piranha cleaning was performed at a ratio of 7:3 of sulfuric acid to hydrogen peroxide, and then, an OTS self-assembled monolayer was formed on the  $\text{SiO}_2$  surface. The polymer films were spin-coated using chloroform solutions ( $7 \text{ mg mL}^{-1}$ ), which was followed by thermal-annealing at different temperatures (as-fabricated; 100 and  $200^\circ\text{C}$ ) for 20 min under an  $\text{N}_2$  atmosphere. The source/drain electrodes (Au, 40 nm) were thermally evaporated at a rate of  $1 \text{ \AA s}^{-1}$ . The channel length ( $L$ ) and width ( $W$ ) were 100 and 1000  $\mu\text{m}$ , respectively.

### 4.4 | Electrical characterizations

Electrical characterization of the OFETs was conducted in high vacuum ( $\sim 10^{-6}$  Torr) using a semiconductor parameter analyzer (Keithley 4200).  $\mu_{\text{h,FET}}$  was evaluated

in saturation regime using the equation,  $I_{D,sat} = (WC_i/2L)\mu_{h,FET}(V_G - V_{th})^2$ , where  $I_{D,sat}$  is the saturated drain current,  $C_i$  ( $10.8 \text{ nF cm}^{-2}$ ) is the capacitance of the gate dielectric,  $V_G$  is the gate voltage, and  $V_{th}$  is the threshold voltage. The sheet resistance of the polymer films was measured using the van der Pauw method, and the electrical conductivity was calculated from the sheet resistance and film thickness. The Seebeck coefficients were measured using a custom-made setup. The setup consists of two Peltier modules that generate a temperature gradient and a thermocouple that simultaneously measures the temperature difference and resulting thermovoltage (Keithley 6510/7700 Data Acquisition System and Keithley 2182 A nanovoltmeter). The AC Hall measurements were performed using an 8404 Hall measurement system (LakeShore), in which an AC magnetic field of frequency 0.01–0.1 Hz and root-mean-square magnitude  $B_{RMS}$  of 1.19 T were used.

#### 4.5 | Other characterizations

$^1\text{H}$  NMR spectra were recorded using a Bruker 300 MHz spectrometer, and  $^{13}\text{C}$  NMR spectra were recorded using a Bruker DRX 500 MHz spectrometer. GPC, equipped with a refractive index detector (eluent: chlorobenzene at a raised temperature of  $60^\circ\text{C}$  with polystyrene standards) was used to obtain  $M_n$  and PDI of polymers. TGA was performed using a TA 2050 TGA thermogravimetric analyzer (TA Instruments) under an  $\text{N}_2$  atmosphere at a heating rate of  $10^\circ\text{C min}^{-1}$ . DSC was conducted under  $\text{N}_2$  atmosphere using a DSC 2100 differential scanning calorimeter (TA Instruments) at a heating rate of  $10^\circ\text{C min}^{-1}$ . UV–Vis–NIR spectra were obtained using a V-770 spectrometer (Jasco). Raman spectra were measured using an Alpha 300 M+ Raman spectrometer (WITEC) with a 532 nm laser source. ESR measurements were performed using a JES-FA200 spectrometer (JEOL). FTIR spectra were measured using an FT/IR-4700 spectrometer (Jasco). Cyclic voltammetry (CV) was performed at room temperature in a 0.1 M solution of tetrabutylammonium perchlorate ( $\text{Bu}_4\text{NClO}_4$ ) in chloroform at a scan rate of  $50 \text{ mV s}^{-1}$ . A Pt wire and an Ag/AgCl electrode were used as the counter and reference electrodes, respectively. 2D GIXD measurements were performed at the 3C and 9A beamlines of the Pohang Accelerator Laboratory (PAL), Korea. AFM images were obtained using an NX-10 atomic force microscope (Park Systems) in the non-contact mode. DFT calculations were performed using the Gaussian 16 package with the non-local hybrid Becke three-parameter Lee–Yang–Parr function and 6-31G\* basis set after the optimization of the molecular geometry.

#### AUTHOR CONTRIBUTIONS

**Hansol Lee:** Conceptualization, methodology, data curation, formal analysis, writing - original draft, writing - review & editing, supervision. **Landep Ayuningtias:** Experimentation, data curation. **Hoimin Kim:** Conceptualization, experimentation, data curation, methodology, validation, formal analysis. **Jaehoon Lee:** Experimentation, data curation. **Jiyun Lee:** Experimentation, data curation. **Min-Jae Kim:** Experimentation, data curation. **Dongki Lee:** Experimentation, data curation. **Byung Mook Weon:** Formal analysis. **Dong-Am Park:** Formal analysis. **Nam-Gyu Park:** Formal analysis. **Sung Yun Son:** Formal analysis. **Junki Kim:** Methodology, supervision. **Yun-Hi Kim:** Methodology, project administration, supervision. **Boseok Kang:** Conceptualization, methodology, validation, project administration, writing - original draft, writing - review & editing, supervision.

#### ACKNOWLEDGMENTS

H.L., L.A., and H.K. contributed equally to this study. This work was supported by National Research Foundation of Korea (NRF) grants funded by the Korean government (NRF 2021R1A2B5B03086367, 2022M3J7A1062940, 2023R1A2C1005015, and RS-2022-00166297). This work was also supported by the International Research & Development Program of the NRF, funded by the Ministry of Science and ICT (2022K1A4A7A04094482). The authors thank the Pohang Accelerator Laboratory for providing the synchrotron radiation sources at the 3C and 9A beamlines used in this study.

#### CONFLICT OF INTEREST STATEMENT

The authors declare no conflict of interest.

#### ORCID

Boseok Kang  <https://orcid.org/0000-0003-4295-3881>

#### REFERENCES

- Meng B, Liu J, Wang L. Recent development of n-type thermoelectric materials based on conjugated polymers. *Nano Mater Sci*. 2021;3(2):113–123. doi:10.1016/j.nanoms.2020.10.002
- Wang H, Yu C. Organic thermoelectrics: materials preparation, performance optimization, and device integration. *Joule*. 2019; 3(1):53–80. doi:10.1016/j.joule.2018.10.012
- Kroon R, Mengistie DA, Kiefer D, et al. Thermoelectric plastics: from design to synthesis, processing and structure-property relationships. *Chem Soc Rev*. 2016;45(22):6147–6164. doi:10.1039/c6cs00149a
- Lee S, Kim S, Pathak A, et al. Recent progress in organic thermoelectric materials and devices. *Macromol Res*. 2020;28(6): 531–552. doi:10.1007/s13233-020-8116-y
- Zhao W, Ding J, Zou Y, Di CA, Zhu D. Chemical doping of organic semiconductors for thermoelectric applications. *Chem Soc Rev*. 2020;49(20):7210–7228. doi:10.1039/d0cs00204f

6. Yuan D, Liu W, Zhu X. Efficient and air-stable n-type doping in organic semiconductors. *Chem Soc Rev.* 2023;52(11):3842-3872. doi:10.1039/d2cs01027e
7. Scheunemann D, Järsvall E, Liu J, et al. Charge transport in doped conjugated polymers for organic thermoelectrics. *Chem Phys Rev.* 2022;3(2):21309. doi:10.1063/5.0080820
8. Boyle CJ, Upadhyaya M, Wang P, et al. Tuning charge transport dynamics via clustering of doping in organic semiconductor thin films. *Nat Commun.* 2019;10(1):2827. doi:10.1038/s41467-019-10567-5
9. Yang K, Chen Z, Wang Y, Guo X. Alkoxy-functionalized bithiophene/thiazoles: versatile building blocks for high-performance organic and polymeric semiconductors. *Acc Mater Res.* 2023;4(3):237-250. doi:10.1021/accountsmr.2c00237
10. George Z, Kroon R, Gehlhaar R, et al. The influence of alkoxy substitutions on the properties of diketopyrrolopyrrole-phenyl copolymers for solar cells. *Materials.* 2013;6(7):3022-3034. doi:10.3390/ma6073022
11. Huang H, Chen Z, Ponce Ortiz R, et al. Combining electron-neutral building blocks with intramolecular "conformational locks" affords stable, high-mobility p- and n-channel polymer semiconductors. *J Am Chem Soc.* 2012;134(26):10966-10973. doi:10.1021/ja303401s
12. Kim HG, Kang B, Ko H, Lee J, Shin J, Cho K. Synthetic tailoring of solid-state order in diketopyrrolopyrrole-based copolymers via intramolecular noncovalent interactions. *Chem Mater.* 2015;27(3):829-838. doi:10.1021/cm503864u
13. Qiu B, Chen S, Xue L, et al. Effects of alkoxy and fluorine atom substitution of donor molecules on the morphology and photovoltaic performance of all small molecule organic solar cells. *Front Chem.* 2018;6:413. doi:10.3389/fchem.2018.00413
14. Song KW, Choi MH, Song HJ, Heo SW, Lee JY, Moon DK. Effect of replacing proton with alkoxy side chain for donor acceptor type organic photovoltaics. *Sol Energy Mater Sol Cells.* 2014;120:303-309. doi:10.1016/j.solmat.2013.09.023
15. Yu ZD, Lu Y, Wang JY, Pei J. Conformation control of conjugated polymers. *Chemistry.* 2020;26(69):16194-16205. doi:10.1002/chem.202000220
16. Lee J, Kim M, Kang B, et al. Side-chain engineering for fine-tuning of energy levels and nanoscale morphology in polymer solar cells. *Adv Energy Mater.* 2014;4(10):1400087. doi:10.1002/aenm.201400087
17. Kim HG, Kim M, Clement JA, et al. Energy level engineering of donor polymers via inductive and resonance effects for polymer solar cells: effects of cyano and alkoxy substituents. *Chem Mater.* 2015;27(19):6858-6868. doi:10.1021/acs.chemmater.5b03256
18. Lee H, Park C, Sin DH, Park JH, Cho K. Recent advances in morphology optimization for organic photovoltaics. *Adv Mater.* 2018;30(34):1800453. doi:10.1002/adma.201800453
19. Liu Z, Hu Y, Li P, Wen J, He J, Gao X. Enhancement of the thermoelectric performance of dpp based polymers by introducing one 3,4-ethylenedioxythiophene electron-rich building block. *J Mater Chem C.* 2020;8(31):10859-10867. doi:10.1039/d0tc01047b
20. Kiefer D, Kroon R, Hofmann AI, et al. Double doping of conjugated polymers with monomer molecular dopants. *Nat Mater.* 2019;18(2):149-155. doi:10.1038/s41563-018-0263-6
21. Li H, Song J, Xiao J, Wu L, Katz HE, Chen L. Synergistically improved molecular doping and carrier mobility by copolymerization of donor-acceptor and donor-donor building blocks for thermoelectric application. *Adv Funct Mater.* 2020;30(40):2004378. doi:10.1002/adfm.202004378
22. Kroon R, Kiefer D, Stegerer D, Yu L, Sommer M, Muller C. Polar side chains enhance processability, electrical conductivity, and thermal stability of a molecularly p-doped polythiophene. *Adv Mater.* 2017;29(24):1700930. doi:10.1002/adma.201700930
23. Liu J, Qiu L, Alessandri R, et al. Enhancing molecular n-type doping of donor-acceptor copolymers by tailoring side chains. *Adv Mater.* 2018;30(7):1704630. doi:10.1002/adma.201704630
24. Huo L, Zhang S, Guo X, Xu F, Li Y, Hou J. Replacing alkoxy groups with alkylthienyl groups: a feasible approach to improve the properties of photovoltaic polymers. *Angew Chem Int ed.* 2011;50(41):9697-9702. doi:10.1002/anie.201103313
25. Xu J, Ji Q, Kong L, Du H, Ju X, Zhao J. Soluble electrochromic polymers incorporating benzoselenadiazole and electron donor units (carbazole or fluorene): synthesis and electronic-optical properties. *Polymers.* 2018;10(4):450. doi:10.3390/polym10040450
26. Bao WW, Li R, Dai ZC, et al. Diketopyrrolopyrrole (DPP)-based materials and its applications: a review. *Front Chem.* 2020;8:679. doi:10.3389/fchem.2020.00679
27. Luo H, Yu C, Liu Z, et al. Remarkable enhancement of charge carrier mobility of conjugated polymer field-effect transistors upon incorporating an ionic additive. *Sci Adv.* 2016;2(5):e1600076. doi:10.1126/sciadv.1600076
28. Ding J, Liu Z, Zhao W, et al. Selenium-substituted diketopyrrolopyrrole polymer for high-performance p-type organic thermoelectric materials. *Angew Chem Int ed.* 2019;58(52):18994-18999. doi:10.1002/anie.201911058
29. Kang I, Yun HJ, Chung DS, Kwon SK, Kim YH. Record high hole mobility in polymer semiconductors via side-chain engineering. *J Am Chem Soc.* 2013;135(40):14896-14899. doi:10.1021/ja405112s
30. Kang K, Watanabe S, Broch K, et al. 2D coherent charge transport in highly ordered conducting polymers doped by solid state diffusion. *Nat Mater.* 2016;15(8):896-902. doi:10.1038/nmat4634
31. Nam G-H, Sun C, Chung DS, Kim Y-H. Enhancing doping efficiency of diketopyrrolopyrrole-copolymers by introducing sparse intramolecular alkyl chain spacing. *Macromolecules.* 2021;54(17):7870-7879. doi:10.1021/acs.macromol.1c01368
32. Li H, DeCoster ME, Ming C, et al. Enhanced molecular doping for high conductivity in polymers with volume freed for dopants. *Macromolecules.* 2019;52(24):9804-9812. doi:10.1021/acs.macromol.9b02048
33. Fujimoto R, Yamashita Y, Kumagai S, et al. Molecular doping in organic semiconductors: fully solution-processed, vacuum-free doping with metal-organic complexes in an orthogonal solvent. *J Mater Chem C.* 2017;5(46):12023-12030. doi:10.1039/c7tc03905k
34. Yurash B, Cao DX, Brus VV, et al. Towards understanding the doping mechanism of organic semiconductors by Lewis acids. *Nat Mater.* 2019;18(12):1327-1334. doi:10.1038/s41563-019-0479-0
35. Kang YH, Ko S-J, Lee M-H, Lee YK, Kim BJ, Cho SY. Highly efficient and air stable thermoelectric devices of poly(3-hexylthiophene) by dual doping of Au metal precursors. *Nano Energy.* 2021;82:105681. doi:10.1016/j.nanoen.2020.105681

36. Wu L, Li H, Chai H, Xu Q, Chen Y, Chen L. Anion-dependent molecular doping and charge transport in ferric salt-doped P3HT for thermoelectric application. *ACS Appl Electron Mater.* 2021;3(3):1252-1259. doi:10.1021/acsaelm.0c01067
37. Lee H, Li H, Kim YS, et al. Novel dithienopyrrole-based conjugated copolymers: importance of backbone planarity in achieving high electrical conductivity and thermoelectric performance. *Macromol Rapid Commun.* 2022;43(19):2200277. doi:10.1002/marc.202200277
38. Min Han J, Eun Yoon S, Hyun Jung K, et al. Dopant-dependent thermoelectric performance of indoloindole-selenophene based conjugated polymer. *Chem Eng J.* 2022;431:133779. doi:10.1016/j.cej.2021.133779
39. Suh EH, Jeong MK, Lee K, et al. Understanding the solution-state doping of donor-acceptor polymers through tailored side chain engineering for thermoelectrics. *Adv Funct Mater.* 2022;32(51):2207886. doi:10.1002/adfm.202207886
40. Sahalianov I, Hynynen J, Barlow S, Marder SR, Muller C, Zozoulenko I. UV-to-IR absorption of molecularly p-doped polythiophenes with alkyl and oligoether side chains: experiment and interpretation based on density functional theory. *J Phys Chem B.* 2020;124(49):11280-11293. doi:10.1021/acs.jpcc.0c08757
41. Suh EH, Kim SB, Yang HS, Jang J. Regulating competitive doping in solution-mixed conjugated polymers for dramatically improving thermoelectric properties. *Adv Funct Mater.* 2022;32(46):2207413. doi:10.1002/adfm.202207413
42. Mendez H, Heimel G, Winkler S, et al. Charge-transfer crystallites as molecular electrical dopants. *Nat Commun.* 2015;6(1):8560. doi:10.1038/ncomms9560
43. Lee JH, Yoon S, Ko MS, Lee N, Hwang I, Lee MJ. Improved performance of organic photovoltaic devices by doping F4TCNQ onto solution-processed graphene as a hole transport layer. *Org Electron.* 2016;30:302-311. doi:10.1016/j.orgel.2016.01.003
44. Untilova V, Biskup T, Biniek L, Vijayakumar V, Brinkmann M. Control of chain alignment and crystallization helps enhance charge conductivities and thermoelectric power factors in sequentially doped P3HT:F4TCNQ films. *Macromolecules.* 2020;53(7):2441-2453. doi:10.1021/acs.macromol.9b02389
45. Tang J, Pai Y-H, Liang Z. Strategic insights into semiconducting polymer thermoelectrics by leveraging molecular structures and chemical doping. *ACS Energy Lett.* 2022;7(12):4299-4324. doi:10.1021/acscenergylett.2c02119
46. Zhong Y, Untilova V, Muller D, et al. Preferential location of dopants in the amorphous phase of oriented regioregular poly(3-hexylthiophene-2,5-diyl) films helps reach charge conductivities of 3000 S cm<sup>-1</sup>. *Adv Funct Mater.* 2022;32(30):2202075. doi:10.1002/adfm.202202075
47. Reiser P, Müller L, Sivanesan V, et al. Dopant diffusion in sequentially doped poly(3-hexylthiophene) studied by infrared and photoelectron spectroscopy. *J Phys Chem C.* 2018;122(26):14518-14527. doi:10.1021/acs.jpcc.8b02657
48. Zhang F, Mohammadi E, Qu G, Dai X, Diao Y. Orientation-dependent host-dopant interactions for manipulating charge transport in conjugated polymers. *Adv Mater.* 2020;32(39):e2002823. doi:10.1002/adma.202002823
49. Wang D, Ding J, Dai X, et al. Triggering ZT to 0.40 by engineering orientation in one polymeric semiconductor. *Adv Mater.* 2023;35(2):e2208215. doi:10.1002/adma.202208215
50. Glauddell AM, Cochran JE, Patel SN, Chabiny ML. Impact of the doping method on conductivity and thermopower in semiconducting polythiophenes. *Adv Energy Mater.* 2015;5(4):1401072. doi:10.1002/aenm.201401072
51. Dongmin Kang S, Jeffrey Snyder G. Charge-transport model for conducting polymers. *Nat Mater.* 2017;16(2):252-257. doi:10.1038/nmat4784

## SUPPORTING INFORMATION

Additional supporting information can be found online in the Supporting Information section at the end of this article.

**How to cite this article:** Lee H, Ayuningtias L, Kim H, et al. From non-doped to dopable: The impact of methoxy functionalization on doping and thermoelectric properties of conjugated polymers. *EcoMat.* 2024;6(4):e12442. doi:10.1002/eom2.12442